JGR Space Physics

RESEARCH ARTICLE
10.1029/2025JA034100

Spatial-Scale Analysis of Rising-Tone Chorus Waves in a Dipole Magnetic Field From Two-Dimensional Particle-in-Cell Simulation

Zhiyang Xia[1], Lunjin Chen[1], Wenyao Gu[1], Xueyi Wang[2], and Huayue Chen[2]

[1]Department of Physics, University of Texas at Dallas, Richardson, TX, USA, [2]Department of Physics, Auburn University, Auburn, AL, USA

Key Points:

- The 2D GCPIC simulation reproduces the generation and propagation of the rising-tone chorus waves in a dipole magnetic field
- The transverse (radial) scale of the chorus element increases from $\sim 15\rho_{e0}$ (electron inertial length) near the equator to $>75\rho_{e0}$ at high latitude
- The parallel scale of the rising tone chorus element is much larger ($>500\rho_{e0}$) than the transverse (radial) scale

Supporting Information:

Supporting Information may be found in the online version of this article.

Correspondence to:

Z. Xia,
Zhiyang.Xia@utdallas.edu

Citation:

Xia, Z., Chen, L., Gu, W., Wang, X., & Chen, H. (2025). Spatial-scale analysis of rising-tone chorus waves in a dipole magnetic field from two-dimensional particle-in-cell simulation. *Journal of Geophysical Research: Space Physics*, *130*, e2025JA034100. https://doi.org/10.1029/2025JA034100

Received 17 APR 2025
Accepted 20 OCT 2025

Abstract We use a two-dimensional particle-in-cell simulation code to examine how the spatial scale evolves as the chorus wave is initially generated in the equatorial source region and then propagates to higher latitudes, experiencing growth or damping while propagating. The distinct rising-tone chorus elements have been successfully excited self-consistently near the magnetic equator within a limited radial region and propagate both outward and inward as the latitude increases. The wave normal angle increases as the latitude increases. We test two types of correlation analyses on both 2D spectra and 1D waveforms to determine the correlation scale of the single rising-tone chorus element. The results indicate that the parallel spatial scale of the chorus element is more than $500\rho_{e0}$ (ρ_{e0} is the electron inertial length at the center of the simulation domain) and the transverse spatial scale increases from $\sim 15\rho_{e0}$ near the equator to $>75\rho_{e0}$ at high latitude. The parallel correlation scale is much larger than the transverse (radial) spatial scale of individual chorus elements, which is consistent with the results of simultaneous multi-satellite observations.

Plain Language Summary The spatial scales of whistler mode chorus waves in the Earth's magnetosphere are related to their generation and affect their propagation and interactions with the energetic electrons in the radiation belts. Previous studies have used simultaneous multi-point VLF wave measurements to investigate the spatial scales of chorus waves. In this study, we use a 2D particle-in-cell simulation code to simulate the excitation and propagation of rising-tone chorus elements in a dipole magnetic field. The simulation can provide detailed information of chorus waves in both the 2D spatial domain and time domain, which can be used to analyze the spatial scale more precisely. The distinct rising-tone chorus elements have been successfully excited near the magnetic equator within a limited radial region and propagate nearly along the background magnetic field line to the high latitude region. The wave propagates mostly outward, and inward propagation also exists. We test two types of spatial scale estimation methods: (a) 2D correlation analysis on wave spectra; (b) 1D correlation analysis on the waveform. Both analyses indicate that the latitudinal spatial scale of the chorus element is much larger than the transverse (radial) spatial scale, which is consistent with the results of simultaneous multi-satellite observations.

1. Introduction

The whistler mode chorus waves are usually observed in the Earth's magnetosphere with discrete structures typically exhibiting rising tones or falling tones in frequency-time spectrogram (Cornilleau-Wehrlin et al., 1978; Gao et al., 2014; Li et al., 2012), which play a dominant role in electron dynamics in the Earth's radiation belts (Bortnik & Thorne, 2007; Horne et al., 2003; Summers et al., 2007; Thorne et al., 2010). The frequency range of chorus waves is typically between 0.1 and 0.8 f_{ce} (where f_{ce} is the equatorial electron gyrofrequency) and usually divided into lower and upper bands by a power gap around 0.5 f_{ce} (Chen, Chen, et al., 2023; Fu et al., 2014; Li et al., 2012; Omura et al., 2009; Tsurutani & Smith, 1974). It is well known that most of the chorus waves are generated near the geomagnetic equator (Lauben et al., 2002; LeDocq et al., 1998; Li et al., 2009; Santolík et al., 2005) and propagate nearly along the background magnetic field (Santolík et al., 2014; Taubenschuss et al., 2016). The whistler mode chorus waves are believed to be excited by cyclotron resonant interaction with energetic (1–50 keV) and anisotropic electrons injected into the inner magnetosphere (Agapitov et al., 2013; Fu et al., 2014; Li et al., 2008, 2010) and the nonlinear interactions with resonant electrons cause their frequency chirping (Chen, Wang, et al., 2023; Gao et al., 2016; Nunn et al., 1997; Omura & Matsumoto, 1982; Omura & Summers, 2006; Tao et al., 2021). Through the wave-particle interactions, chorus waves can accelerate and scatter

electrons, which is the main mechanism for the production of relativistic electrons in the radiation belt (Mourenas et al., 2014; Reeves et al., 2013; Thorne et al., 2013) and makes a primary contribution to electron precipitation into the Earth's atmosphere (Ni et al., 2011; Nishimura et al., 2013; Thorne et al., 2010). To quantify the overall contribution of chorus waves to electron acceleration and losses, it is necessary to determine their characteristic spatial scales, in addition to temporal (or spectral) properties that have been well studied (Tao et al., 2014). Nishimura et al. (2010, 2011) reported that chorus waves could drive pulsating aurora through electron precipitation, and the scale of wave excitation region presumably constrains the spatial extent of the pulsating aurora. Crew et al. (2016) found that individual electron microbursts (at $L \sim 6$) potentially arising from chorus waves map to size scales >120 km at the equator, which may be connected to the scale size of an individual chorus element.

The chorus spatial scales are widely investigated, taking advantage of simultaneous multi-point VLF wave measurements aboard Cluster, THEMIS and Van Allen Probes spacecraft through the time domain correlation technique. Santolík and Gurnett (2003) calculated the correlation of the frequency-averaged power spectral density of discrete chorus elements detected by Cluster spacecraft at L ∼ 4.5 around the magnetic equator, and the obtained correlation coefficient is significant covering 60–260 km parallel and 7–100 km perpendicular (to the background magnetic field) separation. However, in the Earth's outer magnetosphere (L ∼ 10) near the magnetic equator, the spatial correlation scale transverse to the local magnetic field was estimated to be about 3,000 km, according to correlation analysis of the spectral density amplitude integrated on frequency for these chorus elements captured aboard THEMIS spacecraft (Agapitov et al., 2010). In addition, the transverse scale of chorus elements was evaluated to extend up to 600–800 km (for both lower and upper band chorus) through similar correlation analysis of VLF data on Van Allen Probes spacecraft at L ∼ 6 (Agapitov et al., 2017). Besides these individual cases, a statistical analysis based on 11 years (2007–2017) of multi-point wave measurements from THEMIS spacecraft covering $L = 2$–10 suggests the spectral amplitude correlation of lower band chorus emissions remains significant up to 250–800 km transverse range (Agapitov et al., 2018). Using the multi-point wave measurements by two Van Allen Probes in 2013–2019, Agapitov et al. (2021) found that in the region of $L = 2$–6, the spatial scale of chorus wave was about 400–750 km in the transverse direction. Another study (Zhang et al., 2021) based on the Van Allen Probes' observation indicated that the spatial size of chorus waves is less than 433 km at $L <$ ∼6.5. All above chorus spatial scales are obtained based on the correlation of logarithms of chorus spectrogram density averaged or integrated on frequency, and the transverse component is discussed as the single chorus source spatial extent, which is defined as the transverse distance between spacecraft, where the same wave packet can be detected aboard both the spacecraft (Agapitov et al., 2017). Besides estimating the size of chorus wave by using the correlation between wave amplitude observed by multiple spacecraft, another method uses the wave amplitude ratio $\Delta B/\mu B$ (Aryan et al., 2016) and the corresponding statistical studies based on the measurement of two Van Allen Probes over various separation distances illustrated that the average scale of the lower band chorus wave packets varies between ∼1,000 and 2,000 km depending on the intensity and activity of chorus waves and the largest chorus wave packets are generally observed on the dawn-dayside during active geomagnetic conditions where the chorus wave intensity and activity are high (Aryan et al., 2022).

Recently, Shen et al. (2019) used the correlation relationship between the burst mode waveform observations from the two Van Allen Probes to analyze the spatial scale of the fine-scale structured rising tone chorus element. The result showed that the transverse spatial size of the rising tone chorus element is about $\sim 315 \pm 32$ km in the region of $L \sim 5$–6. The size is larger at higher latitudes and larger in the azimuthal direction than in the radial direction. However, analyzing the spatial scale of the chorus wave based on in-situ observations of burst-mode waveforms has very limited distance and time range, cannot distinguish between the spatial and temporal effects, and can only estimate the scale in the direction transverse to the background magnetic field. In this study, we analyze the spatial scales of rising-tone chorus elements in a dipole magnetic field based on the simulation result of a two-dimensional (2D) particle-in-cell (PIC) model. Although the rising-tone chorus waves have been successfully reproduced in 2D PIC simulations (Ke et al., 2017; Lu et al., 2019), their spatial scales have not been investigated. Multi-point spacecraft observations usually require an overall time span for analysis that is much larger than that of a single chorus element to obtain various inter-spacecraft distances. The single chorus source spatial extent obtained through this method may reflect averaged spatial size of many observed chorus elements, which may have different sizes. Fortunately, in 2D PIC simulation it becomes practicable to precisely quantify the spatial size of individual chorus elements since the waveforms on every simulation grid point both along and transverse to (radial direction) the magnetic field lines are available. We assume azimuthal uniformity and

primarily focus on the transverse (radial) scale of chorus waves and we perform a two-dimensional simulation in the meridional plane since the computation for 3D model is unrealistically costly. Our main objective is to investigate how the spatial scale evolves as the chorus wave is initially generated in the equatorial source region and then propagates to higher latitudes, experiencing growth or damping while propagating. The precise spatial scale in kilometers is not the primary focus of this study. Instead, we evaluate the spatial scale in terms of the electron initial length, ρ_{e0}, to allow comparisons with observation.

2. The GCPIC Simulation Model

We use a 2D general curvilinear plasma simulation code (GCPIC) model to study the spatial scales of rising-tone chorus waves in the Earth's inner magnetosphere (Lu et al., 2019; Wang et al., 2024). The main simulation settings can be referred to Wang et al. (2024). The 3D dipole magnetic fields are used. The simulation domain lays in the meridian plane and is represented by 3D curvilinear coordinates (p, q, w). There are 5000 × 400 grids in the p–q plane. The details of the curvilinear coordinates' definition are shown in Lu et al. (2019). Generally speaking, The p coordinate labels dipolar field lines, and increases with increasing L-shell; the q coordinate denotes the position along a dipolar field line, and increases from northern latitudes to southern latitudes along the field lines; and the w coordinate denotes azimuthal direction from west to east and completes the right-handedness of the coordinate system.

In the present simulation, both cold and hot electrons are pushed by the Lorentz force. The fixed ion background is set up to ensure plasma charge neutrality. At the initial state, the cold electron plasma density n_{c0} is proportional to L^{-4} with a temperature of 2 eV. The hot electrons adopt a bi-Maxwellian distribution. At the magnetic equator, the parallel temperature, temperature anisotropy, and the number density of the hot electrons are $T_{\|eq} = 20$ keV, $T_{\perp eq}/T_{\|eq} = 6$, and $n_{heq}/n_{c0} = 0.008$. The radial distribution of the hot electron density is uniform at the equator. The parallel thermal velocity of hot electrons at the magnetic equator is $w_{\|eq} = 0.2c$, where c is the speed of light. The electron distribution along field lines is given according to the conservation of kinetic energy and magnetic moment as:

$$n_h = n_{heq}/\zeta, \tag{1}$$

$$T_{\|} = T_{\|eq}, \tag{2}$$

$$T_{\perp} = T_{\perp eq}/\zeta, \tag{3}$$

where $\zeta = 1 + \left(T_{\perp eq}/T_{\|eq} - 1\right)(1 - B_{eq}/B)$, B is the background magnetic field intensity and B_{eq} is that value at the equator along the same field line. At the center of the simulation domain (Point O in Figure 1), the background magnetic field is $B_{eq,0} = 144$ nT, and the plasma density is $n_{c0} = 5\ \mathrm{cm}^{-3}$, leading to the ratio of cold electron plasma frequency to electron gyrofrequency is $\omega_{pe}/\Omega_{e0} = 5$ there.

The units of time and space are Ω_{e0}^{-1} and $\rho_{e0} = V_{Ae0}/\Omega_{e0}$ (ρ_{e0} is the electron inertial length at the center of the simulation domain), respectively. A reduced system centered at $p = 1639\rho_{e0}$ is used, which corresponds to $L_0 = 0.6$. The simulation domain is in the radial range of $p = 1511$ to $1767\rho_{e0}$ and latitude range of $\lambda = -30°$ to 30°. The average grid lengths are $\Delta p = 0.64\rho_{e0}$ and $\Delta q = 0.32\rho_{e0}$. The time step is $\Omega_{e0}\Delta t = 0.02$. There are 2,200 particles per cell. The absorbing boundary conditions are used for waves and reflecting boundary conditions for particles.

3. Simulation Results

Figure 1 shows the spatial distributions of root mean square (RMS) wave amplitude over time of the B_p magnetic fluctuations (the component in the radial direction) in the modified dipole coordinate (a) and Cartesian geocentric coordinate (b), respectively. The value of the wave magnetic field is normalized by the background magnetic field at the center point $B_{eq,0}$. In Figure 1a, the x-axis is the grid number of the p coordinate that corresponds to a L-shell value (or a dipole magnetic field line) and the y-axis is the grid number of the q coordinate that corresponds to the distance along a magnetic field line. The wave is excited in a limited radial region near the source region (the magnetic equator). This localized excitation of chorus waves occurs due to the combined effects of the decreasing

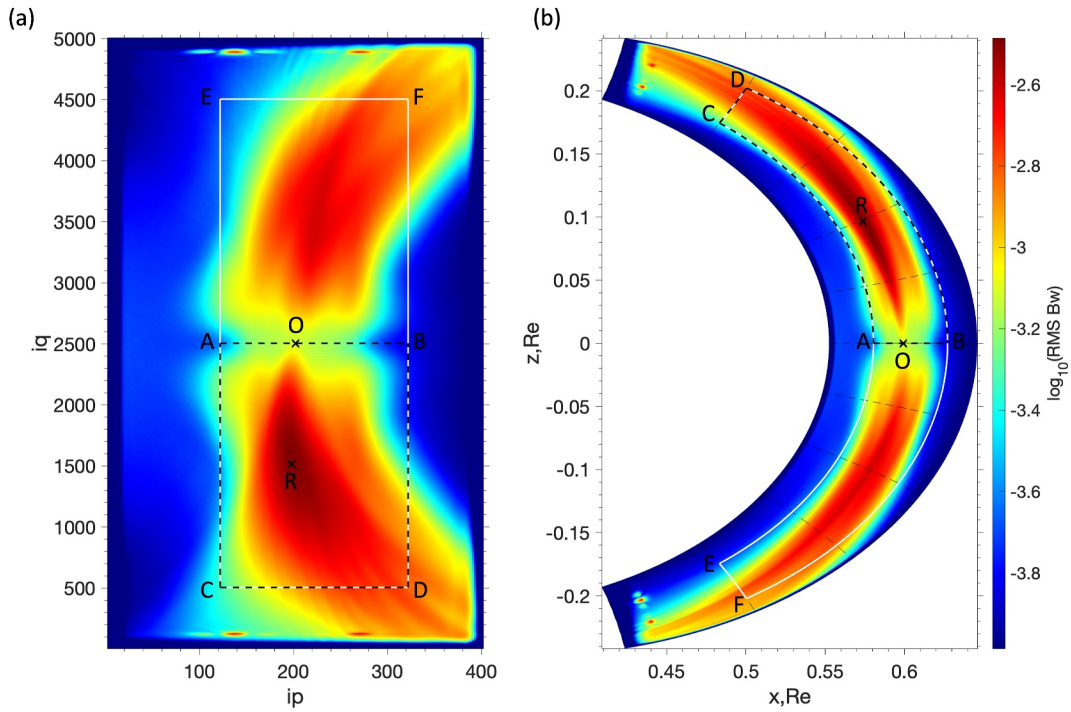

Figure 1. Spatial distributions of root mean square (RMS) wave amplitude over time of the B_p magnetic fluctuations in the modified dipole coordinate (a) and Cartesian geocentric coordinate (b), respectively. The white lines outline the region (CDFE) over which we analyze the spatial distribution of the wave power spectra and wave normal angles, and the black dashed lines outline the region (ABDC) over which the spatial scale analysis is performed. The black crosses label the center point O of the simulation domain and the referring point R for the spatial scale analysis. The grid indexes (ip, iq) of eight selected points are A (121, 2501), B (321, 2501), C (121, 501), D (321, 501), E (121, 4501), F (321, 4501), O (201, 2501) and R (197, 1511).

cold electron density n_{c0} and the increasing ratio of hot to cold electrons n_{heq}/n_{c0} as the L-shell increases. As the wave propagates away from the equator, the wave amplitude increases first and then decreases. In the low latitude region (<~20°), the wave can propagate both outward and inward, and in the higher latitude region (>~20°), the propagation direction is mainly outward. Although the simulation is symmetric between the Northern and Southern Hemispheres, the wave power distribution is not symmetric due to the noise in initial electron distribution and the nature of nonlinear processes of the chorus wave generation. For the following analyses of the wave propagation and spatial scale, we choose one reference point R with the largest RMS wave amplitude, labeled by the black cross in both Figures 1a and 1b. The white lines (CDFE) outline the region in which we analyze the spatial distribution of the wave power and propagation, while the black dashed lines (ABDC) outline the region in which the spatial scale analysis is performed. For each q grid in the ABDC region, we perform a Gaussian fit of the chorus wave amplitude along the p direction and extract three key parameters of the wave amplitude distribution: the peak amplitude, the full width at half maximum (FWHM), and the L-shell corresponding to the amplitude peak. The variations of these parameters with latitude are presented in the Supporting Information S1.

Figure 2 shows the wave power spectra over time (in unit of Ω_{e0}^{-1} of the center point of the simulation domain (Point O in Figure 1) and frequency (in unit of Ω_{e0} of the center point of the simulation domain) at different points in the region outlined by the white lines (CDFE) in Figure 1. The rows stand for different grid numbers in the q direction (iq), and the columns stand for different grid numbers in the p direction (ip). The horizontal magenta dashed lines in each spectrum denote $0.5\Omega_{e0}$, while the white dashed lines denote half of the local electron cyclotron frequency $0.5\Omega_{ce}$. The rising tone chorus element first exists in the region near the equator and then in the high latitude region inside and outside the source field line (represented by the ip value).

We further check the wave normal angle θ_k distribution for these points within the white line region and the results are shown in Figure 3. Signals with low wave power are filtered to highlight the wave normal angle of the chorus

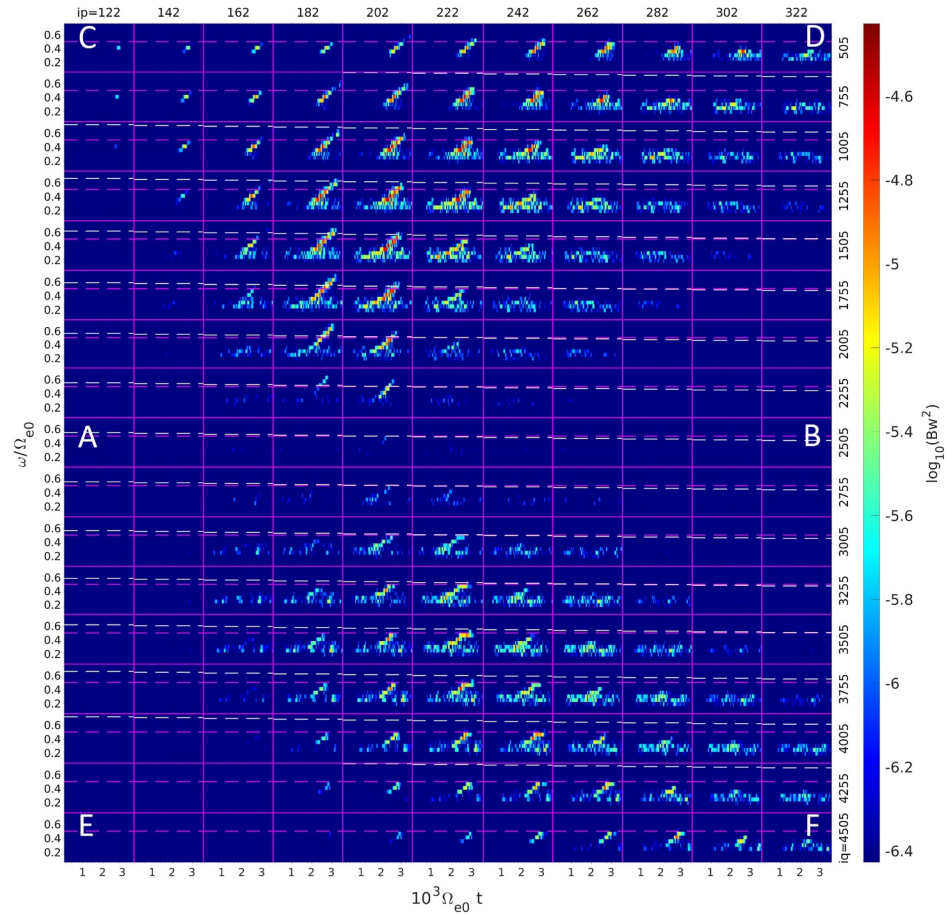

Figure 2. The wave power spectra over time (*x*-axis) and frequency (*y*-axis) at different locations in the region outlined by the white lines in Figure 1. Rows (columns) represent locations with equally spacing grid indexes of p (q) and constant grid indexes of q (p). A, B, C, D, E and F label the six locations along the white line region in Figure 1. Magenta dashed lines denote half electron gyrofrequency at the center point O while black dashed lines denote half local electron gyrofrequency.

element. The values of $0.5\Omega_{ce}$ are denoted by the black dashed lines in this figure and Figure 4. The absolute value of the angle denotes the angle between the vector (wave vector **k** for θ_k) and the background magnetic field line, while the positive sign indicates outward propagation and the negative sign indicates inward propagation. We can see that most of the wave signals propagate outward while some inward propagating signals still exist. As the latitude increases, the outward wave normal angle can become very oblique ($>\sim40°$) while the inward wave normal angles are nearly parallel ($<\sim20°$). The wave normal angle of the high frequency signal is more oblique than that of the low frequency signal. We also calculated the Poynting vector **P** at different points and the distribution of the angle θ_P between **P** and the background magnetic field line is shown in Figure 4. Comparing to the wave normal angle θ_k, the Poynting vector angle θ_P is more parallel ($<\sim20°$). The propagation of the wave packets is less oblique than the propagation of the wave phase. Similar to θ_k, both inward and outward directions of θ_P exist, which indicates the wave packets propagate through different field lines and the radial spatial scale of the wave should increase as the wave propagates from the equator to the high latitude region.

Using the simulated waveform data in the region labeled by the black dashed lines in Figure 1, we perform correlation analysis between the waves at the reference point R and other testing points to estimate the spatial size of the chorus wave element in the meridional plane. Two types of correlation analyses, 2D correlation analysis of the wave power spectra and 1D correlation analysis of the waveform, are performed for the B_p component of the chorus wave, and the results are shown and compared in Figure 5.

Figure 5a shows the wave power spectral density at the reference point (Point R, the black cross in Figure 1) while Figure 5b shows the corresponding waveform. The magenta dashed squares in Figures 5a and 5b denote the time-

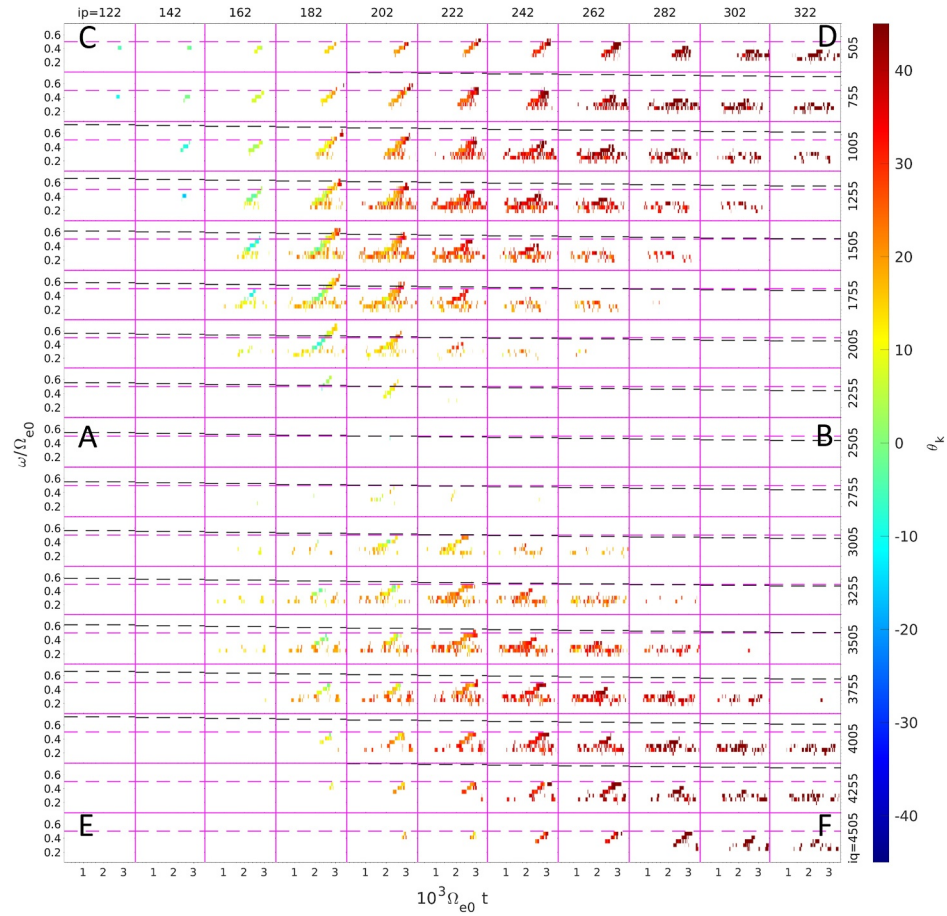

Figure 3. The spatial distribution of the wave normal angle (θ_k) spectra over time (x-axis) and frequency (y-axis) with a similar format to Figure 2. Positive value stands for outward wave normal angle while negative value stands for inward wave normal angle.

frequency domain and time domain for the 2D and 1D correlation analyses, respectively. For the 2D cross-correlation analysis, we evaluate the correlation coefficients between the dynamic spectra at Point R (shown within the magenta box in Figure 5a) and the dynamic spectra (of the same domain as the referenced spectra) at a given location with varying time lags, and then we determine the maximum values of the correlation coefficient (as the correlation coefficient for this location) and corresponding time lag. We will repeat the processes for different locations. For the 1D correlation analysis, similar procedures will be done except that 1D correlation coefficients are calculated between the waveform at Point R (shown within the magenta box in Figure 5b) and the waveform (of the same time duration as the referenced waveform) at a different location with varying time lags. Figure 5c shows the distribution of the 2D correlation coefficient in the meridional plane. The value of the correlation coefficient at each location is the maximum value of the 2D correlation coefficient between the local wave power spectra and the wave spectra at the reference point with different time shifts. The distribution of the corresponding time shift for the maximum correlation coefficient is shown by Figure 5e, where the data points with a correlation coefficient less than 0.7 are removed. The x-z coordinate values are normalized by the electron initial length ρ_{e0} at the center point of the simulation domain. The result shows that the correlation coefficient decreases as the distance between the two points increases in both the parallel (field line) and transverse (radial) directions. The corresponding time shift decreases to negative values as the location becomes closer to the equator and increases to positive values as the latitude increases, which is the consequence of the chorus wave propagating from the equator to the high latitude region. The change of the time shift in the radial direction is not as significant as that in the field line direction. We estimate the spatial scale by the region with high correlation coefficients, as the colored region in Figure 5e. The spatial scale in the field line direction is much larger than in the radial

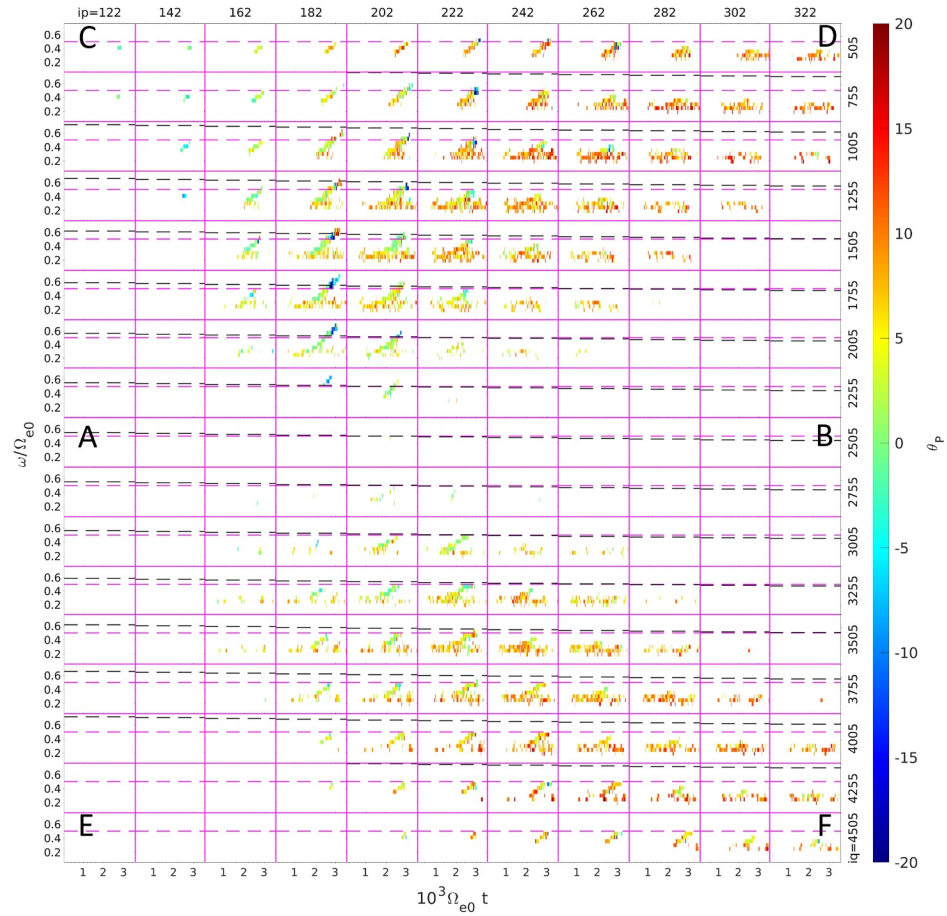

Figure 4. The spatial distribution of the Poynting vector angle (θ_P) spectra over time (x-axis) and frequency (y-axis) with a similar format to Figure 3. Positive value stands for outward Poynting vector while negative value stands for inward Poynting vector.

direction. The parallel scale exceeds the spatial range of our analyzing domain (>500 ρ_{e0}), while the transverse scale increases with latitude, and can reach about 55 ρ_{e0} near point R.

Similar figures for the 1D waveform correlation analysis are shown in Figures 5d and 5f. For the 1D correlation analysis, the maximum correlation coefficient decreases more rapidly in radial and parallel directions than the 2D correlation coefficient. Another important feature of the 1D correlation coefficient distribution is that although the correlation coefficient decreases overall as the distance to the reference point increases in the field line direction, the variation is not monotonically decreasing and includes some periodic oscillations, which can be seen as the cell structures in Figure 5d. A possible reason for this oscillation of the correlation coefficient is the frequency dispersion. The frequency variation of the chorus element leads to different propagation time delays for different frequencies between the two locations along the wave propagation, due to the frequency-dependent group velocity of whistler-mode waves. As a result, the phase difference between time series at two locations is not a constant (i.e., depending on time). A high degree of correlation (or a high correlation coefficient) however would require a constant time lag between the waveforms. This leads to a strong perturbation of cross-correlation coefficient (showing a quasi-periodic distribution with maximum and minimum values) even within the spatial structure of the same chorus element. When determining the spatial scale from waveforms between multiple nearby satellites, if this 1D cross-correlation analysis is used, the apparent coefficient oscillation may lead to the underestimation of the spatial size of chorus waves. Therefore, we suggest using the 2D cross-correlation analysis of the wave power spectra to estimate the spatial scale of the chorus element.

From the spatial scale analyses mentioned above, which used a fixed reference point (Point R in Figure 1), both radial and field-aligned displacement from Point R contributes to the degree of correlation. To separate the

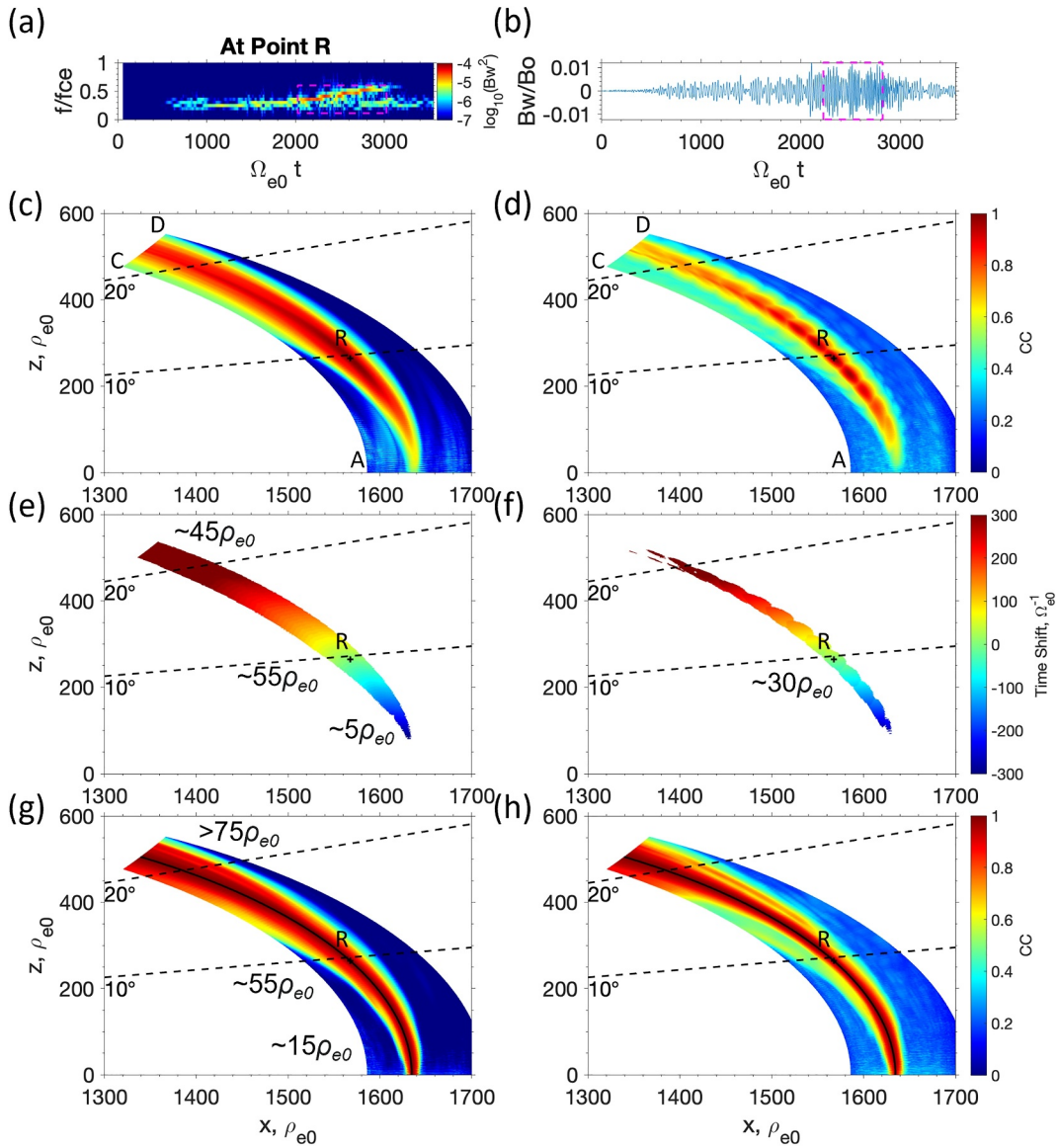

Figure 5. The spatial scale analysis results for the 2D wave spectra correlation analysis and the 1D waveform analysis. (a) Is the wave spectra at the referring point R and (b) is the waveform at the referring point R. (c) Is the spatial distribution of the maximum correlation coefficient of the 2D wave spectra against the 2D wave spectra at the fixed reference location R (marked by the magenta box in panel (a)), and (e) is the spatial distribution of the time shifts corresponding to the maximum correlation coefficients in panel (c). Letters A, C, and D in panel (c) denote the points along the black dashed lines in Figure 1. The data points with correlation coefficients less than 0.7 are filtered from (e). (d, f) Are spatial distributions of maximum correlation coefficients and time shifts but for the 1D waveform correlation analysis against the waveform at the fixed reference R (marked by the magenta box in panel (b)). Panels (g, h) are spatial distributions of maximum correlation coefficients for the 2D wave spectra cross-correlation and 1D waveform cross-correlation with a spatially varying reference along the referenced field line passing through R. The black dashed lines represent the latitudes of 10° and 20°, respectively.

variation of correlation coefficients in radial and parallel directions, we choose a varying reference point, depending on the location of interest for correlation analysis. The reference point R′ has the same q as that location and has the same p value as Point R (i.e., R′ is along the referenced magnetic field line passing through Point R). The resulting distributions of the 2D and 1D correlation coefficients on the meridional plane are shown in Figures 5g and 5h. The black solid lines in Figures 5g and 5h denote the referenced magnetic field line through Point R. Compared with the correlation coefficients for the fixed reference point (Figures 5c and 5d), the value of cross-correlation coefficients is larger when using this moving reference point. This is reasonable since the

parallel displacement from the reference point is removed, and thus, the contribution of the frequency dispersion to the correlation analysis is minimized. As a result, the calculated spatial scale also increases. The parallel scale exceeds the domain of the analysis ($\sim 500\rho_{e0}$); the transverse scale increases from $\sim 15\rho_{e0}$ at the equator to $>75\rho_{e0}$ as latitude increases. Another noticeable difference is that for the fixed reference point, the spatial scale of 1D correlation analysis decreases in the higher latitude region (Figure 5d). However, for the moving reference point, the spatial scale of 1D correlation analysis significantly increases and becomes comparable to the spatial scale of 2D correlation analysis. One more interesting point is that the cell structures of 1D correlation analysis (Figure 5d) vanish for the moving reference point case, which suggests that these cell structures are mainly caused by the propagation effect (frequency dispersion).

For the estimated spatial scales of the chorus wave, we are also interested in comparing them to the wavelength of the chorus wave. We use the cold dispersion relation to estimate the parallel wavelength of the chorus wave. The average estimated parallel wavelength with 20° wave normal angle is about 10 ρ_{e0} for frequency from $0.2\Omega_{ce}$ to $0.6\Omega_{ce}$. Thus, the transverse scale of chorus elements is in the order of about 1–10 of the parallel wavelength.

4. Summary and Discussion

In this paper, using a 2D GCPIC simulation code, we reproduce the generation and propagation of rising-tone chorus waves in a dipole magnetic field and analyze the spatial size of a single rising-tone chorus element. Taking advantage of 2D PIC simulation, where the waveforms on every grid point are available, we extract the spatial extent of a single chorus wave packet. Two types of correlation analyses are used to quantify the similarity of chorus elements over different locations: (a) correlation coefficient of the 2D spectral density matrix in the frequency and time dimensions, (b) correlation coefficient of the 1D waveform in the time dimension. Both analyses take into account the time delay caused by wave propagation. Our main conclusions are summarized below:

1. The distinct rising-tone chorus elements have been successfully excited self-consistently in our simulation. They are first generated near the magnetic equator within a narrow radial region and then propagate toward high latitudes nearly along the magnetic field line. Most chorus emissions propagate outward, and as the wave propagates to higher latitude regions, the wave normal angle becomes more oblique. Inward propagation also exists near the high-latitude region.
2. The analysis of the spatial size of the single rising-tone chorus element yields that the transverse scale of chorus waves increases with latitude, ranging from $\sim 15\rho_{e0}$ near the equator up to $>75\rho_{e0}$ at high latitude.
3. The parallel (field line aligned) spatial scale $(>500\rho_{e0})$ is much larger than the transverse scale from both the 2D correlation analysis of the wave spectra and the 1D correlation of the waveform.

The parallel scale of chorus waves being much larger than the transverse scale is consistent with the results from simultaneous multi-satellite observations of chorus elements (Breneman et al., 2009; Santolík et al., 2004). Comparing the two kinds of correlation analysis, the 2D correlation coefficient of the wave spectra decreases more slowly as the distance between two chorus elements increases. The variation of the 1D correlation coefficient of the waveform is not monotonic and oscillates as the distance between two elements increases. The reason for this oscillation of the 1D correlation coefficient may be associated with the frequency dispersion. This oscillation of the 1D correlation coefficient may cause the underestimation of spatial scale while using multi-point in situ observation to determine the spatial scale of the rising tone chorus and is more suitable for the spatial scale estimation of the waves with a nearly fixed frequency. For the waves with frequency dispersion, we suggest using the 2D correlation coefficient of the wave spectra for the spatial scale estimation. In this study based on the 2D GCPIC simulation results, the transverse spatial scale of the rising-tone chorus element determined by the 2D correlation analysis can reach $>75\ \rho_{e0}$ and the parallel spatial scale is larger than $500\ \rho_{e0}$. The parallel correlation scale ($500\ \rho_{e0}$) corresponds to about 1,200 km in the Earth's magnetosphere, which is comparable to the observational statistical result of about 1,500 km (Shen et al., 2019). On the other hand, the transverse spatial scale ($75\ \rho_{e0}$) corresponds to about 180 km, which is comparable to the result around 100 km at L ~ 4 in Santolík and Gurnett (2003) but less than the existing statistical results, about 315 km at L ~ 5–6 in Shen et al. (2019) and about 400–750 km at L ~ 2–6 in Agapitov et al. (2021) based on Van Allen Probes data. Our main goal in this study is to investigate how the spatial scale evolves as the chorus wave is initially generated in the equatorial source region and then propagates to higher latitudes, where the wave experiences growth or damping. The precise spatial scale in kilometers and the comparison to the estimation from in space experiment is not the primary focus of this study

for the following two reasons: (a) Previous chorus wave spatial scale studies based on spacecrafts' observation either used low resolution survey mode wave observation which cannot distinguish each chorus element (Agapitov et al., 2021; Aryan et al., 2022; Zhang et al., 2021) or used high resolution burst mode observation but did not strictly ensure that the chorus waves observed by two spacecrafts are the same individual chorus element (Shen et al., 2019). Our simulation generates a single chorus element, so the corresponding spatial scale is expected to be smaller than those derived from in situ observations. (b) The spatial scale estimation is dependent on the choice of critical values used for cross-correlation coefficients (or other similarity metrics), and different observation or analysis methods using different thresholds can lead to uncertainty in the estimated scales. For two-point cross-correlation studies using spacecraft observations, 2D correlation analysis of the wave spectra is a more effective approach, particularly when analyzing high-resolution measurements of chorus waves where frequency chirping can be clearly observed. Estimates of spatial scales may vary across studies due to several contributing factors, including the spacecraft separation, the performance and calibration of measurement instruments, the data quality, the cross-correlation analysis technique employed, and the threshold criteria selected. These considerations are important to account for when evaluating and comparing spatial scale results of chorus waves reported in different studies.

In reality, the source region of chorus waves can exhibit inhomogeneity in both radial and azimuthal directions (Agapitov et al., 2021; Shen et al., 2019). The transverse scales estimated from in situ observations include both radial and azimuthal components, with the radial component potentially varying along the azimuthal direction. However, due to the constraints of the 2D simulation domain, our study assumes a uniform source particle distribution in the azimuthal direction, effectively treating the azimuthal spatial scale as infinite. Consequently, the transverse scale considered in our study includes only the radial component and remains uniform in the azimuthal direction. One may interpret the radial scale simulated in our current study as the radial scale of the source region on the meridional plane corresponding to the center of the source region, and in this sense, the simulated radial scale could represent the radial scale of the 3D source region of chorus waves. A 3D simulation model is required to examine the azimuthal spatial scale of chorus element distribution; however currently it is not feasible due to computational limit. It's worth noting that due to computation limitation, the topology of the background magnetic field in our simulation domain around $L \sim 0.6$ is chosen, although the plasma parameters used in the simulation are typical values at $L \sim 5$–6 in the Earth's magnetosphere. Thus our model reproduces chorus-like elements with frequency chirping but does not capture all the features of naturally occurring chorus emissions. How the inhomogeneity and curvature of the magnetic field affect the spatial scale of chorus elements is left for future work.

Conflict of Interest

The authors declare no conflicts of interest relevant to this study.

Data Availability Statement

The data of the 2D GCPIC simulation can be downloaded from Xia (2024).

Acknowledgments
We acknowledge the support of NASA Grants 80NSSC21K1688, 80NSSC23K0089, 80NSSC24K0174, 80NSSC25K7749, 80NSSC21K1320 and the AFOSR Grant FA9550-23-1-0568. The work at Auburn University was supported by the NASA Grants 80NSSC24K0174 and 80NSSC21K1679, the NSF Grant AGS-2131012, and the NSF EPSCoR OIA-2148653.

References

Agapitov, O., Artemyev, A., Krasnoselskikh, V., Khotyaintsev, Y. V., Mourenas, D., Breuillard, H., et al. (2013). Statistics of whistler mode waves in the outer radiation belt: Cluster STAFF-SA measurements. *Journal of Geophysical Research: Space Physics*, *118*(6), 3407–3420. https://doi.org/10.1002/jgra.50312

Agapitov, O., Blum, L. W., Mozer, F. S., Bonnell, J. W., & Wygant, J. (2017). Chorus whistler wave source scales as determined from multipoint Van Allen Probe measurements. *Geophysical Research Letters*, *44*(6), 2634–2642. https://doi.org/10.1002/2017GL072701

Agapitov, O., Krasnoselskikh, V., Zaliznyak, Y., Angelopoulos, V., Le Contel, O., & Rolland, G. (2010). Chorus source region localization in the Earth's outer magnetosphere using THEMIS measurements. *Annales Geophysicae*, *28*(6), 1377–1386. https://doi.org/10.5194/angeo-28-1377-2010

Agapitov, O., Mourenas, D., Artemyev, A., Breneman, A., Bonnell, J. W., Hospodarsky, G., & Wygant, J. (2021). Chorus and hiss scales in the inner magnetosphere: Statistics from high-resolution filter bank (FBK) Van Allen Proves multi-point measurements. *Journal of Geophysical Research: Space Physics*, *126*(7), e2020JA028998. https://doi.org/10.1029/2020JA028998

Agapitov, O., Mourenas, D., Artemyev, A., Mozer, F. S., Bonnell, J. W., Angelopoulos, V., et al. (2018). Spatial extent and temporal correlation of chorus and hiss: Statistical results from multipoint THEMIS observations. *Journal of Geophysical Research: Space Physics*, *123*(10), 8317–8330. https://doi.org/10.1029/2018JA025725

Aryan, H., Bortnik, J., Sibeck, D. G., & Hospodarsky, G. (2022). Global map of chorus wave sizes in the inner magnetosphere. *Journal of Geophysical Research: Space Physics*, *127*(3), e2021JA029768. https://doi.org/10.1029/2021JA029768

Aryan, H., Sibeck, D., Balikhin, M., Agapitov, O., & Kletzing, C. (2016). Observation of chorus waves by the Van Allen Probes: Dependence on solar wind parameters and scale size. *Journal of Geophysical Research: Space Physics*, *121*(8), 7608–7621. https://doi.org/10.1002/2016JA022775

Bortnik, J., & Thorne, R. (2007). The dual role of ELF/VLF chorus waves in the acceleration and precipitation of radiation belt electrons. *Journal of Atmospheric and Solar-Terrestrial Physics*, *69*(3), 378–386. https://doi.org/10.1016/j.jastp.2006.05.030

Breneman, A. W., Kletzing, C. A., Pickett, J., Chum, J., & Santolik, O. (2009). Statistics of multispacecraft observations of chorus dispersion and source location. *Journal of Geophysical Research*, *114*(A6). https://doi.org/10.1029/2008JA013549

Chen, H., Chen, R., Gao, X., Lu, Q., Ke, Y., & Kong, Z. (2023). Unraveling the role of electron Plateau distributions in the power gap formation of chorus waves: Van Allen Probes observations. *Geophysical Research Letters*, *50*(6), e2023GL102748. https://doi.org/10.1029/2023GL102748

Chen, H., Wang, X., Chen, L., Omura, Y., Tsurutani, B. T., Lin, Y., & Xia, Z. (2023). Evolution of chorus subpackets in the Earth's magnetosphere. *Geophysical Research Letters*, *50*(21), e2023GL105938. https://doi.org/10.1029/2023GL105938

Cornilleau-Wehrlin, N., Gendrin, R., Lefeuvre, F., Parrot, M., Grard, R., Jones, D., et al. (1978). VLF electromagnetic waves observed onboard GEOS-1. *Space Science Reviews*, *22*(4), 371–382. https://doi.org/10.1007/BF00210874

Crew, A. B., Spence, H. E., Blake, J. B., Klumpar, D. M., Larsen, B. A., O'Brien, T. P., et al. (2016). First multipoint in situ observations of electron microbursts: Initial results from the NSF firebird II mission. *Journal of Geophysical Research: Space Physics*, *121*(6), 5272–5283. https://doi.org/10.1002/2016JA022485

Fu, X., Cowee, M. M., Friedel, R. H., Funsten, H. O., Gary, S. P., Hospodarsky, G. B., et al. (2014). Whistler anisotropy instabilities as the source of banded chorus: Van Allen Probes observations and particle-in-cell simulations. *Journal of Geophysical Research: Space Physics*, *119*(10), 8288–8298. https://doi.org/10.1002/2014JA020364

Gao, X., Li, W., Thorne, R. M., Bortnik, J., Angelopoulos, V., Lu, Q., et al. (2014). New evidence for generation mechanisms of discrete and hiss-like whistler mode waves. *Geophysical Research Letters*, *41*(14), 4805–4811. https://doi.org/10.1002/2014GL060707

Gao, X., Mourenas, D., Li, W., Artemyev, A. V., Lu, Q., Tao, X., & Wang, S. (2016). Observational evidence of generation mechanisms for very oblique lower band chorus using THEMIS waveform data. *Journal of Geophysical Research: Space Physics*, *121*(7), 6732–6748. https://doi.org/10.1002/2016JA022915

Horne, R. B., Glauert, S. A., & Thorne, R. M. (2003). Resonant diffusion of radiation belt electrons by whistler-mode chorus. *Geophysical Research Letters*, *30*(9). https://doi.org/10.1029/2003GL016963

Ke, Y., Gao, X., Lu, Q., Wang, X., & Wang, S. (2017). Generation of rising-tone chorus in a two-dimensional mirror field by using the general curvilinear pic code. *Journal of Geophysical Research: Space Physics*, *122*(8), 8154–8165. https://doi.org/10.1002/2017JA024178

Lauben, D. S., Inan, U. S., Bell, T. F., & Gurnett, D. A. (2002). Source characteristics of ELF/VLF chorus. *Journal of Geophysical Research*, *107*(A12), SMP10-1–SMP10-17. https://doi.org/10.1029/2000JA003019

LeDocq, M. J., Gurnett, D. A., & Hospodarsky, G. B. (1998). Chorus source locations from VLF poynting flux measurements with the polar spacecraft. *Geophysical Research Letters*, *25*(21), 4063–4066. https://doi.org/10.1029/1998GL900071

Li, W., Thorne, R. M., Angelopoulos, V., Bortnik, J., Cully, C. M., Ni, B., et al. (2009). Global distribution of whistler-mode chorus waves observed on the THEMIS spacecraft. *Geophysical Research Letters*, *36*(9). https://doi.org/10.1029/2009GL037595

Li, W., Thorne, R. M., Bortnik, J., Nishimura, Y., Angelopoulos, V., Chen, L., et al. (2010). Global distributions of suprathermal electrons observed on THEMIS and potential mechanisms for access into the plasmasphere. *Journal of Geophysical Research*, *115*(A12). https://doi.org/10.1029/2010JA015687

Li, W., Thorne, R. M., Bortnik, J., Tao, X., & Angelopoulos, V. (2012). Characteristics of hiss-like and discrete whistler-mode emissions. *Geophysical Research Letters*, *39*(18). https://doi.org/10.1029/2012GL053206

Li, W., Thorne, R. M., Meredith, N. P., Horne, R. B., Bortnik, J., Shprits, Y. Y., & Ni, B. (2008). Evaluation of whistler mode chorus amplification during an injection event observed on CRRES. *Journal of Geophysical Research*, *113*(A9). https://doi.org/10.1029/2008JA013129

Lu, Q., Ke, Y., Wang, X., Liu, K., Gao, X., Chen, L., & Wang, S. (2019). Two-dimensional GCPIC simulation of rising-tone chorus waves in a dipole magnetic field. *Journal of Geophysical Research: Space Physics*, *124*(6), 4157–4167. https://doi.org/10.1029/2019JA026586

Mourenas, D., Artemyev, A. V., Agapitov, O. V., & Krasnoselskikh, V. (2014). Consequences of geomagnetic activity on energization and loss of radiation belt electrons by oblique chorus waves. *Journal of Geophysical Research: Space Physics*, *119*(4), 2775–2796. https://doi.org/10.1002/2013JA019674

Ni, B., Thorne, R. M., Shprits, Y. Y., Orlova, K. G., & Meredith, N. P. (2011). Chorus-driven resonant scattering of diffuse Auroral electrons in nondipolar magnetic fields. *Journal of Geophysical Research*, *116*(A6). https://doi.org/10.1029/2011JA016453

Nishimura, Y., Bortnik, J., Li, W., Thorne, R. M., Chen, L., Lyons, L. R., et al. (2011). Multievent study of the correlation between pulsating aurora and whistler mode chorus emissions. *Journal of Geophysical Research*, *116*(A11). https://doi.org/10.1029/2011JA016876

Nishimura, Y., Bortnik, J., Li, W., Thorne, R. M., Lyons, L. R., Angelopoulos, V., et al. (2010). Identifying the driver of pulsating aurora. *Science*, *330*(6000), 81–84. https://doi.org/10.1126/science.1193186

Nishimura, Y., Bortnik, J., Li, W., Thorne, R. M., Ni, B., Lyons, L. R., et al. (2013). Structures of dayside whistler-mode waves deduced from conjugate diffuse aurora. *Journal of Geophysical Research: Space Physics*, *118*(2), 664–673. https://doi.org/10.1029/2012JA018242

Nunn, D., Omura, Y., Matsumoto, H., Nagano, I., & Yagitani, S. (1997). The numerical simulation of VLF chorus and discrete emissions observed on the Geotail satellite using a Vlasov code. *Journal of Geophysical Research*, *102*(A12), 27083–27097. https://doi.org/10.1029/97JA02518

Omura, Y., Hikishima, M., Katoh, Y., Summers, D., & Yagitani, S. (2009). Nonlinear mechanisms of lower-band and upper-band VLF chorus emissions in the magnetosphere. *Journal of Geophysical Research*, *114*(A7). https://doi.org/10.1029/2009JA014206

Omura, Y., & Matsumoto, H. (1982). Computer simulations of basic processes of coherent whistler wave-particle interactions in the magnetosphere. *Journal of Geophysical Research*, *87*(A6), 4435–4444. https://doi.org/10.1029/JA087iA06p04435

Omura, Y., & Summers, D. (2006). Dynamics of high-energy electrons interacting with whistler mode chorus emissions in the magnetosphere. *Journal of Geophysical Research*, *111*(A9). https://doi.org/10.1029/2006JA011600

Reeves, G. D., Spence, H. E., Henderson, M. G., Morley, S. K., Friedel, R. H. W., Funsten, H. O., et al. (2013). Electron acceleration in the heart of the Van Allen radiation belts. *Science*, *341*(6149), 991–994. https://doi.org/10.1126/science.1237743

Santolík, O., Gurnett, D., Pickett, J., Parrot, M., & Cornilleau-Wehrlin, N. (2005). Central position of the source region of storm-time chorus. *Planetary and Space Science*, *53*(1), 299–305. https://doi.org/10.1016/j.pss.2004.09.056

Santolík, O., & Gurnett, D. A. (2003). Transverse dimensions of chorus in the source region. *Geophysical Research Letters*, *30*(2). https://doi.org/10.1029/2002GL016178

Santolík, O., Gurnett, D. A., & Pickett, J. S. (2004). Multipoint investigation of the source region of storm-time chorus. *Annales Geophysicae*, *22*(7), 2555–2563. https://doi.org/10.5194/angeo-22-2555-2004

Santolík, O., Macúšová, E., Kolmašová, I., Cornilleau-Wehrlin, N., & de Conchy, Y. (2014). Propagation of lower-band whistler-mode waves in the outer Van Allen belt: Systematic analysis of 11 years of multi-component data from the cluster spacecraft. *Geophysical Research Letters*, *41*(8), 2729–2737. https://doi.org/10.1002/2014GL059815

Shen, X.-C., Li, W., Ma, Q., Agapitov, O., & Nishimura, Y. (2019). Statistical analysis of transverse size of lower band chorus waves using simultaneous multisatellite observations. *Geophysical Research Letters*, *46*(11), 5725–5734. https://doi.org/10.1029/2019GL083118

Summers, D., Ni, B., & Meredith, N. P. (2007). Timescales for radiation belt electron acceleration and loss due to resonant wave-particle interactions: 2. Evaluation for VLF chorus, ELF hiss, and electromagnetic ion cyclotron waves. *Journal of Geophysical Research*, *112*(A4). https://doi.org/10.1029/2006JA011993

Tao, X., Bortnik, J., Albert, J. M., Thorne, R. M., & Li, W. (2014). Effects of discreteness of chorus waves on quasilinear diffusion-based modeling of energetic electron dynamics. *Journal of Geophysical Research: Space Physics*, *119*(11), 8848–8857. https://doi.org/10.1002/2014JA020022

Tao, X., Zonca, F., & Chen, L. (2021). A "trap-release-amplify" model of chorus waves. *Journal of Geophysical Research: Space Physics*, *126*(9), e2021JA029585. https://doi.org/10.1029/2021JA029585

Taubenschuss, U., Santolík, O., Breuillard, H., Li, W., & Le Contel, O. (2016). Poynting vector and wave vector directions of equatorial chorus. *Journal of Geophysical Research: Space Physics*, *121*(12), 11912–11928. https://doi.org/10.1002/2016JA023389

Thorne, R. M., Li, W., Ni, B., Ma, Q., Bortnik, J., Chen, L., et al. (2013). Rapid local acceleration of relativistic radiation-belt electrons by magnetospheric chorus. *Nature*, *504*(7480), 411–414. https://doi.org/10.1038/nature12889

Thorne, R. M., Ni, B., Tao, X., Horne, R. B., & Meredith, N. P. (2010). Scattering by chorus waves as the dominant cause of diffuse auroral precipitation. *Nature*, *467*(7318), 943–946. https://doi.org/10.1038/nature09467

Tsurutani, B. T., & Smith, E. J. (1974). Postmidnight chorus: A substorm phenomenon. *Journal of Geophysical Research (1896–1977)*, *79*(1), 118–127. https://doi.org/10.1029/JA079i001p00118

Wang, X., Chen, H., Omura, Y., Hsieh, Y.-K., Chen, L., Lin, Y., et al. (2024). Resonant electron signatures in the formation of chorus wave subpackets. *Geophysical Research Letters*, *51*(8), e2023GL108000. https://doi.org/10.1029/2023GL108000

Xia, Z. (2024). Data for spatial scales of rising-tone chorus in a dipole magnetic field: Two-dimensional particle-in-cell simulation [Dataset]. *Zenodo*. https://doi.org/10.5281/zenodo.12709164

Zhang, S., Rae, I. J., Watt, C. E. J., Degeling, A. W., Tian, A., Shi, Q., et al. (2021). Determining the global scale size of chorus waves in the magnetosphere. *Journal of Geophysical Research: Space Physics*, *126*(11), e2021JA029569. https://doi.org/10.1029/2021JA029569